# Array-Based Seismic Measurements of OSIRIS-REx's Re-Entry

Fernando, Benjamin A.; Charalambous, Constantinos; Schmerr, Nick; Craig, Timothy J.; Wolf, Jonathan; Lewis, Kevin; Sansom, Eleanor K.; Saliby, Christelle; McCleary, Meaghan; Inman, Jennifer; LaPierre, Justin; Giannone, Miro Ronac; Pearson, Karen; Fleigle, Michael; Larmat, Carene; Karatekin, Ozgur; Hanson, Lavender Elle; Baliyan, Shivani; Buttsworth, David; Cheng, Hiu Ching Jupiter; Chinchalkar, Neeraja S.; et al.



**To be published in:** Seismological Research Letters

**DOI to publisher's version:** 10.1785/0220240339





**Focus Section:** OSIRIS-REx

# Array-Based Seismic Measurements of OSIRIS-REx's Re-Entry

Benjamin A. Fernando* *et al.*

## Abstract

**The return home of the OSIRIS-REx spacecraft in September 2023 marked only the fifth time that an artificial object entered the Earth's atmosphere at interplanetary velocities. Although rare, such events serve as valuable analogs for natural meteoroid re-entries; enabling study of hypersonic dynamics, shock wave generation, and acoustic-to-seismic coupling. Here, we report on the signatures recorded by a dense (100 m scale) 11-station array located almost directly underneath the capsule's point of peak atmospheric heating in northern Nevada. Seismic data are presented, which allow inferences to be made about the shape of the shock wave's footprint on the surface, the capsule's trajectory, and its flight parameters.**

**Cite this article as** Fernando, B. A., C. Charalambous, N. Schmerr, T. J. Craig, J. Wolf, K. Lewis, E. K. Sansom, C. Saliby, M. McCleary, J. Inman, *et al.* (2025). Array-Based Seismic Measurements of OSIRIS-REx's Re-Entry, *Seismol. Res. Lett.* **XX**, 1–11, doi: 10.1785/0220240339.

## Introduction

### Sample return capsules and seismoacoustics

Sample return capsules arriving from deep space are the only artificial objects that re-enter the Earth's atmosphere at speeds and trajectories comparable to natural meteoroids. This makes them ideal for studying hypersonic re-entry dynamics as said capsules have known mass, dimension, speed, and trajectory (Silber *et al.*, 2023). Because they have known parameters, they can serve as controlled analogs for natural objects during the entry, descent, and landing (EDL) phase of the mission.

In seismoacoustic studies of meteor phenomena, the atmospheric shock waves and low-frequency sound produced by natural meteoroids re-entering the atmosphere are used to identify and track them on either infrasound sensors or seismometers (e.g., Edwards *et al.*, 2008). The complexities of shock wave generation and propagation down through the turbulent atmosphere (and coupling into the ground in the case of seismic recordings) mean that recordings of hypersonic capsules acting as "artificial meteoroids" are particularly valuable in understanding the seismoacoustic processes involved.

Such events are rare, having occurred only four times on Earth previously. ReVelle *et al.* (2005) made seismic and acoustic measurements of the National Aeronautics and Space Administration's (NASA) Genesis spacecraft's EDL, and ReVelle and Edwards (2007) did the same for NASA's Stardust. More recently, comparable measurements were made during the EDLs of two JAXA missions, Hayabusa and Hayabusa2 (Yamamoto *et al.*, 2011; Sansom *et al.*, 2022).

The potential value of such recordings for being able to study shock wave propagation and air-to-ground coupling in particular also resulted in two (unsuccessful) attempts by NASA's InSight spacecraft to record EDLs seismoacoustically on Mars, of NASA's Mars 2020 mission (Fernando, Wójcicka, Froment, *et al.*, 2021, 2022) and China's Tianwen-1 (Fernando, Wójcicka, Han, *et al.*, 2021).

### The OSIRIS-REx mission

In September 2023, the OSIRIS-REx (ORX) sample return capsule became the fifth artificial object to re-enter the Earth's atmosphere at interplanetary speeds. With many improvements in instrumentation having been made since Stardust's landing in 2006, the ORX EDL presented an ideal opportunity to make seismoacoustic measurements of an "artificial meteoroid" re-entry over a similar geographical area to two previous missions.

A number of different teams took part in this instrumentation campaign, using both ground-based and airborne infrasound sensors, and conventional and optical seismometers. For a full review of the instruments deployed as part of this campaign see Silber *et al.* (2024). Fernando *et al.* (2024) presented initial results from a separate part of this observation campaign, using a single seismic acoustic station 50 km from the array described in this article at a site called Fish Creek from which the data were live-streamed over the internet.

### EDL profile

In this section, we briefly describe the planned trajectory of ORX between the atmospheric interface and peak heating. Note that all times and locations are based on prelanding model predictions (e.g., Ajluni *et al.*, 2015), as a postlanding "as-flown" trajectory has not yet been released.

Atmospheric interface was due to occur over the Pacific Ocean, west of San Francisco, California, at 14:41:55 UTC

Full author list and affiliations appear at the end of this article.

*Corresponding author: bfernan9@jh.edu

on Sunday, 24 September 2023. The defined altitude of interface was 132 km, at which time the spacecraft was expected to be traveling at Mach ~25 (43,000 km/hr; 11.9 km/s).

At the point of peak atmospheric heating from frictional drag, the capsule was expected to be in the mesosphere at around 62 km altitude over 39.5585° N, 116.3852° W in northern Nevada. This is a relatively remote region with no permanent seismometers within several dozen kilometers, and we are not aware of any publicly accessible infrasound stations within the wider area. This necessitated the deployment of these temporary seismic arrays.

Temperatures during peak heating were expected to reach ~3100 K at a speed of Mach 30 (39,000 km/hr; 10.8 km/s) and a deceleration approaching 300 $m/s^2$ (31 g). Note that the Mach number at peak heating is higher than at the atmospheric interface despite the capsule's deceleration, due to the increase in sound speed with altitude through the thermosphere.

As the point of peak heating is where the maximum amount of energy is being dissipated into the atmosphere, the expectation was for an intense shock wave to be generated in this area. This shock was expected to transition to a linear acoustic wave during propagation down through the atmosphere and be audible at the surface as a sonic boom.

On a seismic network, the sonic booms themselves are primarily recorded via the production of an itinerant strain field in response to the surface loading and unloading from wavefront-induced compression and rarefaction (Kanamori *et al.*, 1992). Small contributions to the observed displacement after the initial motion may also come about from more complex effects, such as compliance-induced ground deformation (Sorrells, 1971; Kenda *et al.*, 2020).

## Instrumentation campaign

The deployment discussed in this article involved eleven individual seismic stations, each consisting of a three-axis Fairfield ZLand 3C node set to 24 dB gain and 2000 samples per second.

The deployment location for these nodes was chosen to be as close to the point of projected peak heating as possible, to try to capture the shock wave at its strongest point. For natural meteoroids, peak emission is expected to occur around the point of peak heating, and hence measurements made of artificial capsules in this region of flight are of particular interest as analogs.

The array was located at Bean Flats, on U.S. Bureau of Land Management land, in an area shared with large herbivorous creatures (cows). Despite the presence of topographic variation in the wider region, this area itself was very flat, with less than 4 m of undulation between the array's center and edge in any direction. Given a sound speed in the air of ~330 m/s, this corresponds to a very small elevation-induced correction to phase arrival times, on the order of 0.01 s.

Instruments were deployed in a cross-shaped array, with an instrument spacing of ~100 m. This configuration, and wider geographical context, are shown in Figure 1 alongside the ORX EDL trajectory. The long axis of the array was chosen to be parallel to ORX's trajectory footprint.

Each instrument was manually leveled and pointed toward north using multiple compasses as references, with errors in orientation estimated to be less than ±2°. The reported Global Positioning System coordinates of each station are the mean of readings made on multiple handheld instruments.

The sensors were buried with their tops a few centimeters below the ground's surface to reduce environmental noise. Some of the surface covering was removed by rain and wind (and possibly the actions of the previously mentioned herbivores) between deployment and collection. Signals from instrument 4 (the most uprange) were found to be particularly noisy. The ground at this location was ascertained to be soft, mostly dry superficial alluvium. Detailed geophysical surveys from this area of Nevada suggest soil properties described by $V_P = 585$ m/s and $V_S = 350$ m/s, Poisson ratio = 0.22, and Young's Modulus $E = 0.45$ MPa (Allander and Berger, 2009).

## Seismic data

Data were recorded at all eleven stations, and are shown in Figure 2 and in detail for one station in Figure 3. Seismograms were processed by removing the instrument response and Butterworth-band-pass filtering between 1 and 100 Hz. The beam shown in Figure 4a,c uses a slightly broader frequency range, 2–200 Hz.

## Detailed *N*-wave structure

A clear, rounded (smoothed) *N*-wave signature is observed just after 14:46:04.5 UTC. A downward, near-instantaneous first motion associated with the acoustic compression is followed by an upward ground motion associated with the atmospheric rarefaction.

The rounding of the *N* wave is characteristic of a shock wave which has decayed in the turbulent atmosphere (in particular the planetary boundary layer) to become a linear sound wave, though retaining its characteristic *N*-wave shape in a more rounded form (Pierce and Maglieri, 1972; Ben-Menahem and Singh, 1981; Plotkin, 2002). The arrival time is commensurate with the expected capsule overflight a few minutes previously (around 14:42 UTC). The overall duration of the *N*-wave phase within the wavetrain is around 0.15 s, depending on which station is examined and how the end of the rarefaction period is chosen (we use the first zero-crossing after the rarefaction).

Differences are observed in the structure of the rounded *N* wave (Fig. 2), even between stations that are separated by only 100 m. Frequencies up to 500 Hz are recorded at some stations (e.g., 2 and 10), while others (e.g., 1 and 3) are limited to the highest frequencies around 400 Hz. The rarefaction has a narrower frequency content than the compression and is accordingly broader.

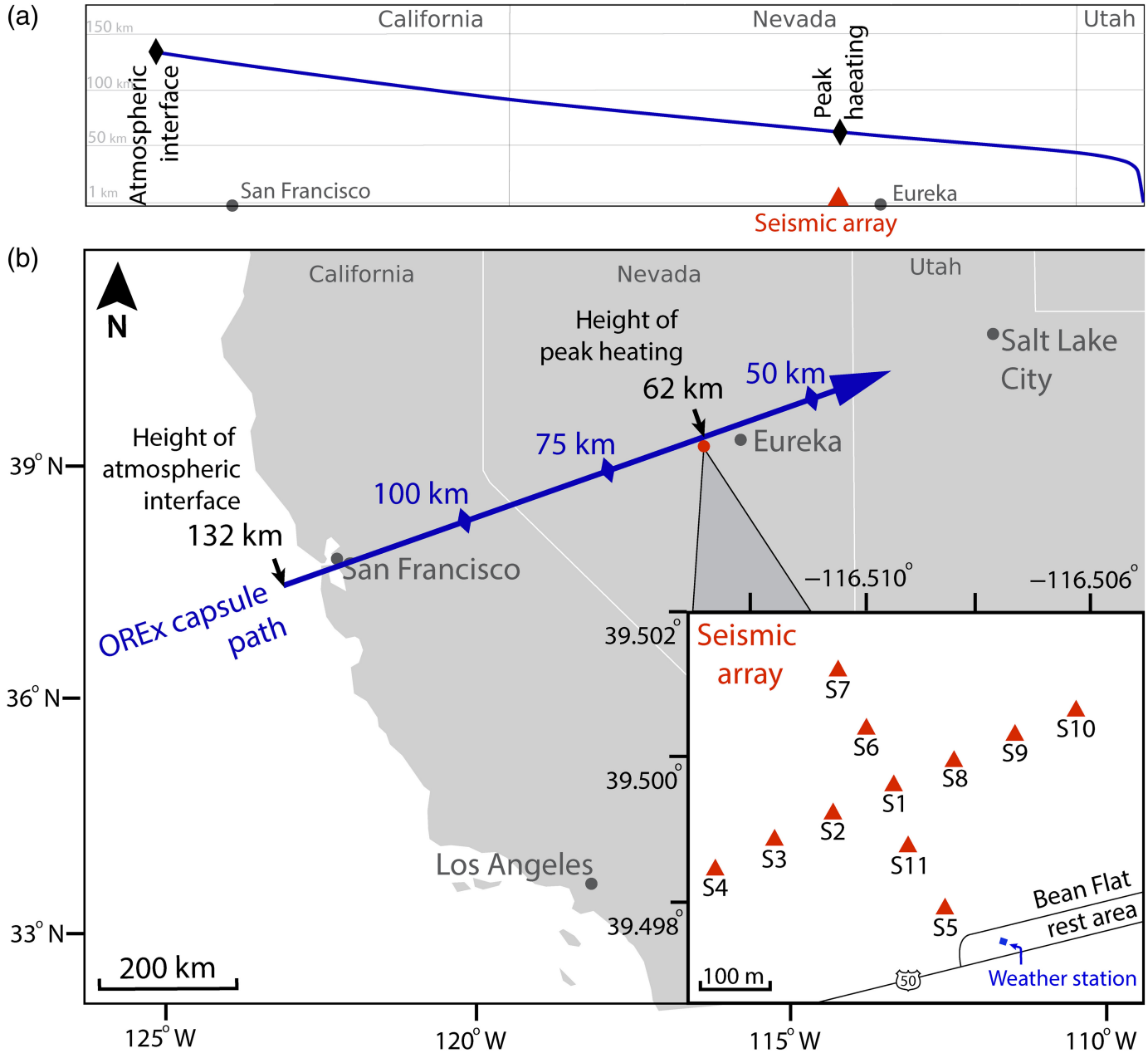


The most significant origins of these differences are likely propagation effects associated with inhomogeneity and turbulence in the atmosphere (Pierce and Maglieri, 1972) and local variations in sediment properties (causing different coupling behavior, McDonald and Goforth, 1969). The spatially varying nature of the seismic source itself (i.e., the fact that the capsule is descending and decelerating over time) may also have had a small effect.

We now consider a more detailed analysis of the signal recorded at a single station, as shown in Figure 3. These data are for station 1, as it is located at the array center, but similar features are recorded across the array.

As per Figure 3a, the *N* wave is most clearly detectable on the vertical component, as is expected for a wavefront traveling almost vertically downward (McDonald and Goforth, 1969). A peak ground velocity of $2.6 \times 10^6$ m/s is noted, which is slightly higher than that noted by Fernando *et al.* (2024) of $2.0 \times 10^6$ at a site 50 km away.

**Figure 1.** (a) The OSIRIS-REx (ORX) entry, descent, and landing (EDL) trajectory (side view), from the point of atmospheric interface to landing. (b) Geographical context (top-down view) of the trajectory. We refer to directions toward landing as "downrange" and those toward the atmospheric interface as "uprange." The inset panel shows the seismometer array deployment. Note that the long arm of the array is parallel to the expected trajectory (i.e., runs uprange/downrange). The cross arm is perpendicular to the trajectory (i.e., cross-range). The lateral distance between the center line of the array and the trajectory footprint on the ground is ~2300 m. The color version of this figure is available only in the electronic edition.

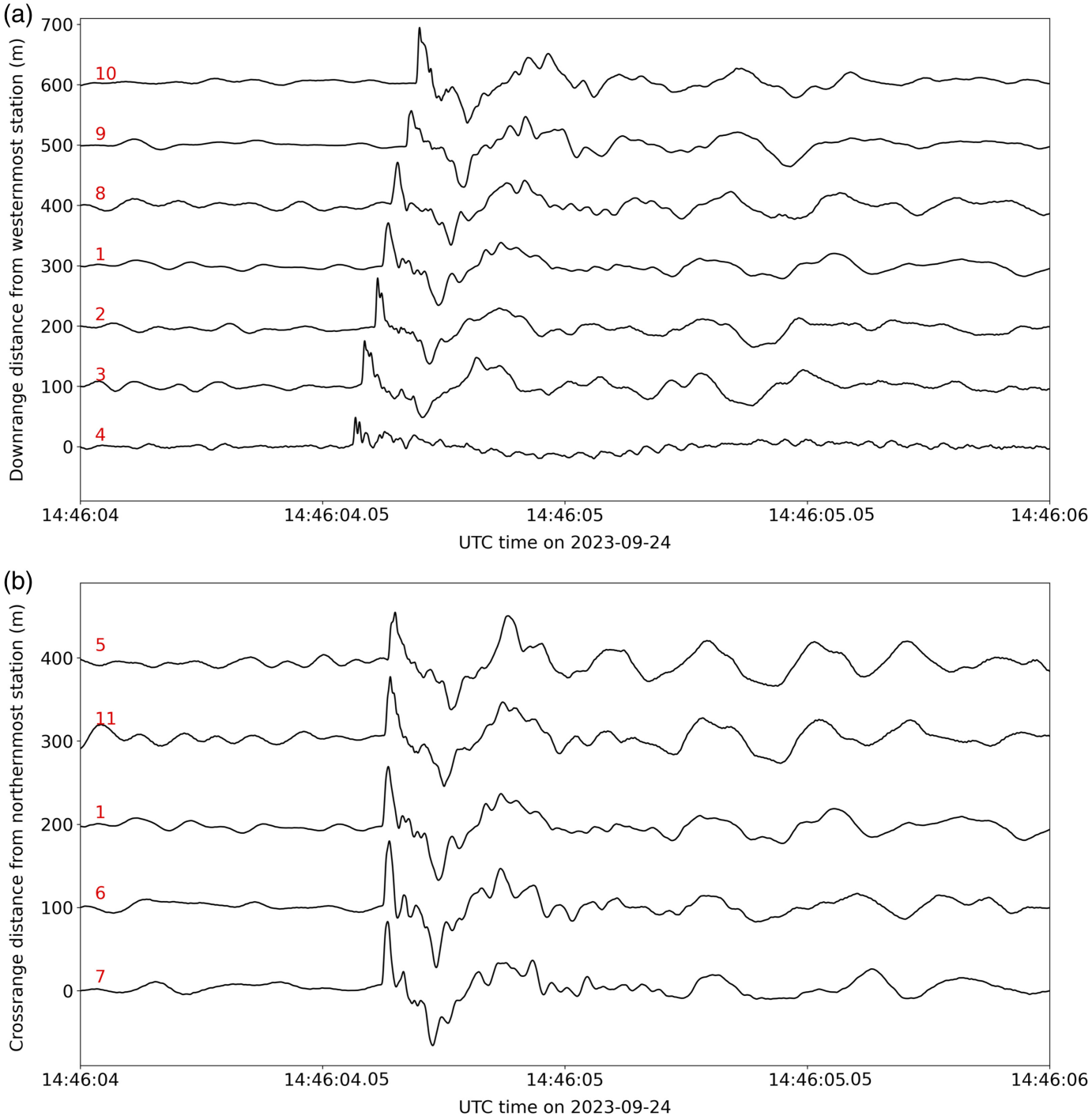


**Figure 2.** The array records seismic data. Traces are vertical ground velocity in the 1–100 Hz range and are arranged in (a) by downrange distance from the westernmost station in the array and in (b) by cross-range distance from the northernmost station. Station numbers are indicated in red on the left side. The weak signal at station 4 is thought to be due to issues with the instrument, which displayed higher noise levels throughout the deployment. The color version of this figure is available only in the electronic edition.

Figure 3b shows a vertical-component spectrogram. Weak background noise with energy predominantly at frequencies up to 30 Hz is apparent before the rounded *N*-wave arrival. The amplitude variations across the array (higher noise levels closer to the road), the moveout of the energy, and the identification of similar signatures in the seismic record at a later time (15:25–15:27 UTC) collectively indicate a vehicular origin for this particular noise source. This is discussed further in the Traffic Data section.

Finally, Figure 3c shows the ground particle motion associated with the initial *N* wave (orange) and the rest of the wavetrain (blue). The overwhelmingly vertical motion associated with the *N* wave is clear. A potential elliptical polarization can be seen in the rest of the wavetrain, suggesting the presence of Rayleigh waves here.

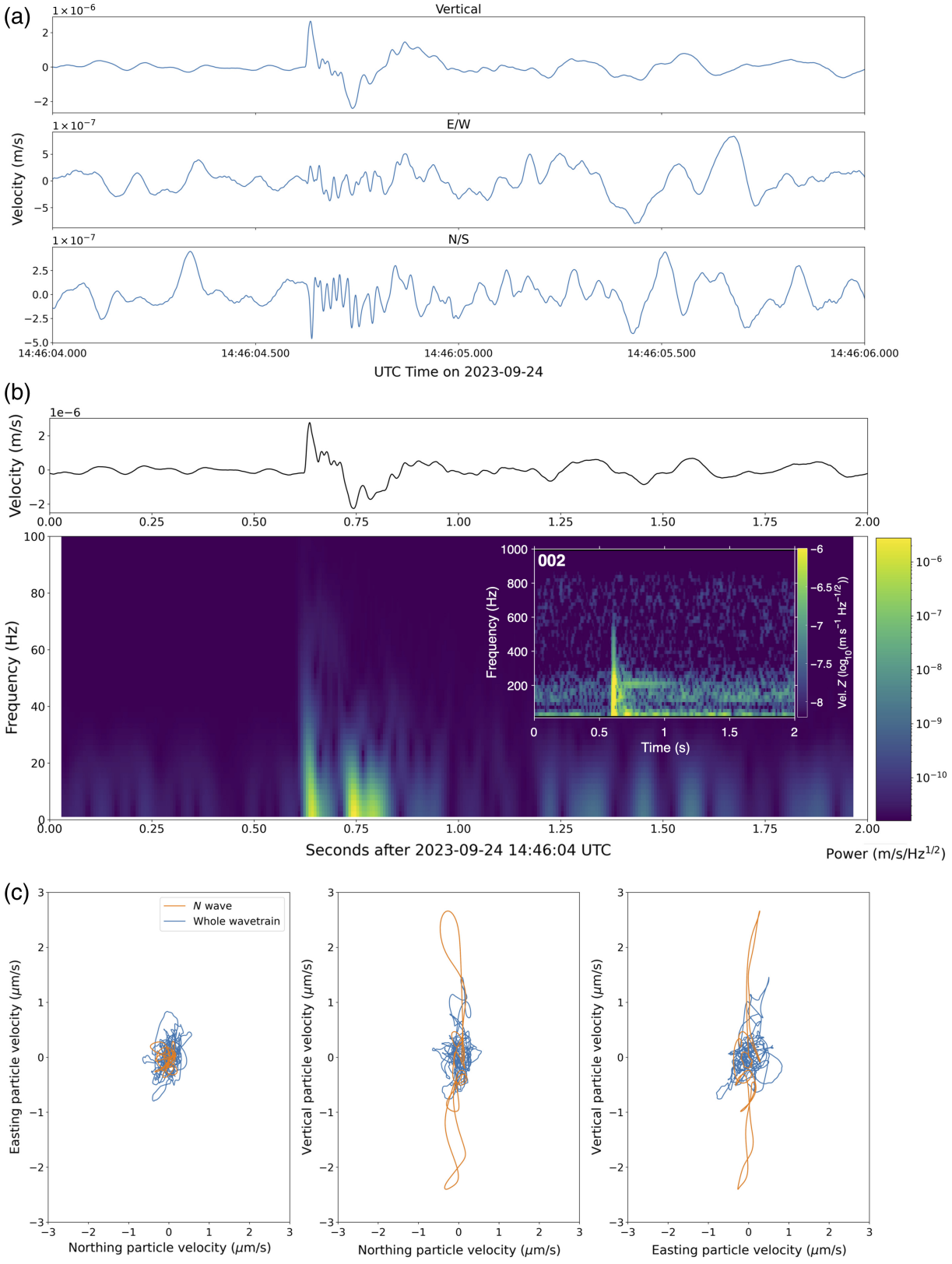


**Figure 3.** Data from the central station of the array (station 1), band passed between 1 and 100 Hz. The *N* wave is only clearly apparent on the vertical component. (a) Three-component data shows the dominance of the signal on the vertical component. (b) Velocity spectrogram for the vertical component. A small inset is shown for station 2 (one station uprange from station 1), to illustrate the variation in peak frequency recorded between stations. At station 2, a resonance around 200 Hz is also observed, which could correspond to excitation in a thin playa layer around 1–2 m thick. (c) Particle motion, with the *N* wave shown in orange (14:46:04.4–14:46:04.8 UTC) and the remainder of the wavetrain in blue. The color version of this figure is available only in the electronic edition.

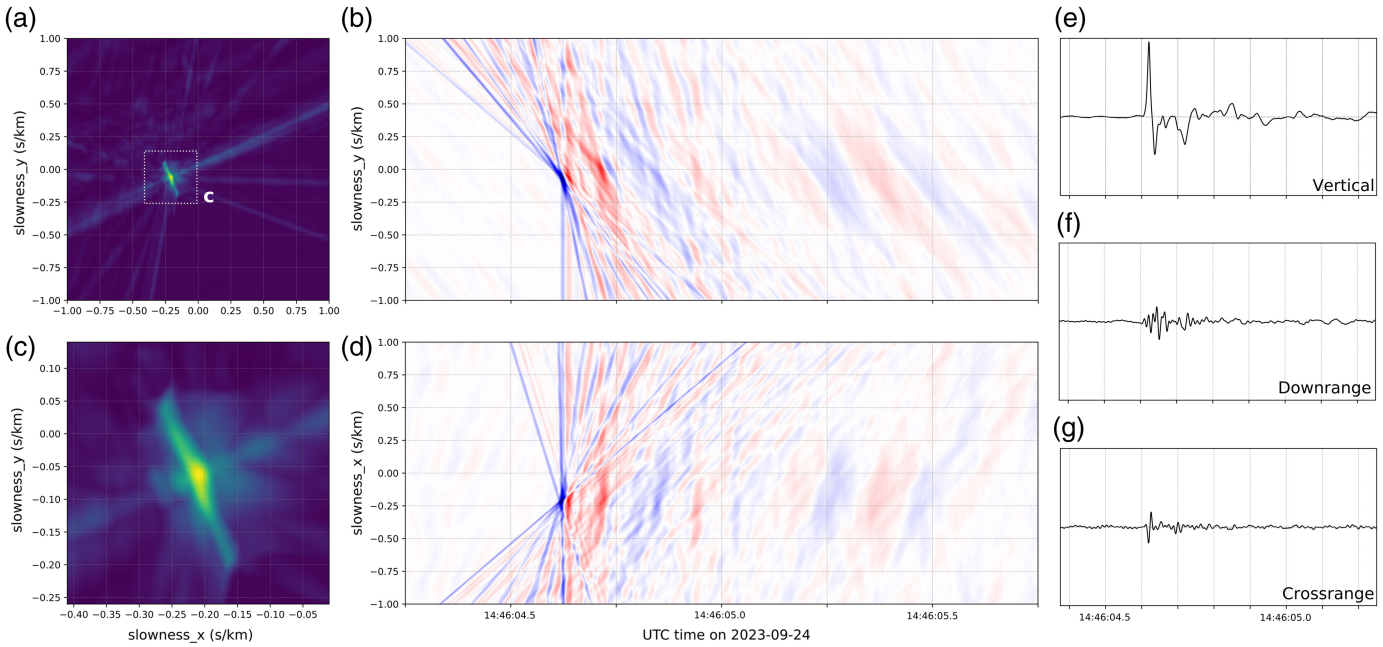


**Figure 4.** Array analysis of the ORX re-entry signal. (a,c) The results of a beam pack through slowness in *x* and *y*, taking the maximum amplitude with ±50 samples (0.025 s) of the absolute maximum amplitude for the shockwave arrival (at 14:46:04.621 and a slowness of [−0.209, −0.063]). (b,d) Vespagrams in *y* and *x* slowness space, respectively. In each vespagram, the other slowness is fixed at the value giving the absolute maximum amplitude for the shock wave arrival. All plots are normalized to the peak value. (e–g) The optimal-slowness beam for vertical, downrange, and cross-range components, respectively, in the pass band 1–100 Hz. All beams are normalized to the peak value of the vertical component beam. The color version of this figure is available only in the electronic edition.

**Slowness and origin azimuth.** In considering the passage of the sonic boom over the array, it is important to consider that the capsule does not act as a point source. Rather, while traveling at supersonic speeds it is more appropriately described as a line source producing a conical shock front (Carlson and Maglieri, 1972). The opening angle of the cone, $\mu$, is given by

$$\mu = \arcsin\frac{1}{M}, \tag{1}$$

in which $M$ is the Mach number, in this case 30—corresponding to an opening angle of 1.9°. This narrow Mach cone means that the seismic source may effectively be considered to be a cylinder (Karakostas *et al.*, 2018). The acoustic rays themselves are emitted at the complement of the Mach angle (Cates and Sturtevant, 2002), which in this case is 88.1°, that is, nearly normal to the shock front.

The intersection of the Mach cone with the ground produces a hyperbola along which a sonic boom is audible, and the passage of the hyperbola over the surface sweeps out a sonic boom "carpet." As per equation (1), the hyperbolic footprint also becomes narrower with increasing Mach number.

In Figure 4, we first show the results of a beam pack aimed at determining the 2D slowness of the overpressure wavefront, followed by vespagrams showing beams in slowness $s_x$ and $s_y$ space. These are constructed under the assumption that the wave propagates across the array as a plane wave at a consistent velocity. We do not find it necessary to compensate for the small variation in topographic elevation across the array as this is <4 m across an array aperture of ~600 m and hence the impact of elevation variation is small.

The beam pack shows the maximum arrival amplitude with a 0.025 s window around the overall maximum amplitude stack, as a function of slowness in the east ($s_x$) and north ($s_y$) directions. As Figure 4a,c shows, there is a clear peak in amplitude associated with wavefront arrival at a slowness of $[s_x,s_y] = [-0.209, -0.063]$. The actual signal is convolved with an array response function leading to amplitude artifacts associated with the orientation of the arms of the array in the uprange and cross-range directions, these are visible as bright lines in the beam pack. The fact that the array response function passes slightly northwest of [0,0] in slowness space indicates the array was slightly to the south of the actual re-entry trajectory (consistent with prelanding predictions, and indicating that the spacecraft was either on or ever so slightly south of its nominal re-entry line).

The 2D slowness of the wavefront arrival indicates that the point of apparent wavefront emission is at an azimuth of 253° (roughly west-southwest), and an apparent slowness of 0.214 s/km. The derived azimuth is very close to the prelanding nominal prediction of 249°. The beam pack is extremely well resolved, given the frequency of the overpressure wave and array aperture. The vespagrams in Figure 4b,d show evidence for either a slight variation in slowness across

the array, or equivalently, the detection of wavefront curvature. In this case, where source-array distance is likely to be only around two orders of magnitude higher than the array aperture, slight wavefront curvature is more likely than the impact of a consistent atmospheric gradient on the length scale of the array aperture. The former would also be expected given that the sonic boom footprint on the ground is a hyperbola.

**Source location analysis.** Given the azimuth and slowness resolution of the array, we are also able to estimate origin location of the shock wave. Without a full atmospheric model and inversion of the data, which are beyond the scope of this article, this involves making a number of assumptions.

First, we assume that the sonic boom can be represented as a plane wave propagating through the atmosphere, which, as we justify above, is an approximation, which is reasonable in the far field. Second, we assume that the shock wave has decayed sufficiently such that it propagates at the speed of sound $v_0$, which we calculate to be 332 m/s (see the Weather data section for more details on this calculation).

Geometrically, we consider the apparent slowness ($s_{\text{app}} = \frac{1}{v_{\text{app}}}$) of the wavefront across the array (e.g., Rost and Thomas, 2002) as

$$s_{\text{app}} = \frac{\sin\theta}{v_0}. \tag{2}$$

In the downrange direction, the apparent velocity $v_{\text{app}}$ of the wavefront across the array is 4581 m/s. Note that this is an apparent, rather than physical, velocity and yields an estimated angle of emission which is 4.15° from the vertical. This is the equivalent point-source angle of emission, and does not reproduce the actual, extended line source nature of the capsule as a seismic source; but it does indicate that the signal was produced almost exactly overhead the array, as expected. When combined with the derived bearing from the previous section of 253°, this indicates an origin for the shock wave, which is slightly to the southwest of the array and almost vertically above it. Note that this result also suggests that the effects of atmospheric refraction of the acoustic rays are minimal, as each different layer of the vertically stratified atmosphere is encountered at a near-normal angle to its interface.

**Pre- and post-cursors.** Similarly to Fernando *et al.* (2024), no clear precursor phases are noted, and there are no coherent sources detected by our array. This is as expected because precursors are normally restricted to settings where the supersonic source is "slow" as compared to the compressional speed in the ground, such that surface waves induced immediately beneath the source can "overtake" a slower direct airwave due to the higher wavespeeds in the ground (Cook and Goforth, 1970). In this case, the capsule's velocity is very much greater than $V_P$, thus explaining the absence of precursor phases (McDonald and Goforth, 1969). Furthermore, the sound speed in the ground is only slightly higher (less than factor 2) than the sound speed in the air.

We do note that there is an increase in noise levels around 14:45:50 UTC, around twenty seconds before the ORX signal (see the Traffic Data section for more details). We exclude this as being a precursor, as it arrives too early as compared to the airwave and has a moveout consistent with a vehicular origin, specifically a lorry/truck that arrived at the nearby rest area and idled until 14:47 UTC.

Conversely, a relatively rich set of seismic waves is apparent immediately after the initial rounded *N* wave. These are visible as an extended set of oscillations in Figure 2a,b. These have similar slowness to the airwave arrival, and hence are potentially associated with acoustic waves propagating in the atmosphere after the initial compression/rarefaction, or longer-duration complex deformation associated with the wavefront's passage over the station. It is also likely that Rayleigh waves are present in this wavetrain. Given that $V_S$ in playa is extremely close to the sound-speed in air, the air-to-ground coupling should be strong. However, this closeness of speeds also makes phase separation challenging.

**Comparison to known flight parameters.** In theory, the detailed seismic recordings made at this array could be inverted for the capsule's trajectory and flight parameters. However, this is extremely challenging in practice, due to the lack of an exact atmospheric state model or an as-flown trajectory.

Nonetheless, we note that a comparison of the boom duration ($\tau$) to theoretical predictions given by Kanamori *et al.* (1992) is possible. Following the approach of Whitham (1974) (though with slightly different notation, and correction for a missing exponent noted by Kanamori *et al.*, 1992), given a capsule speed $u$ at height $h$ we expect $\tau$ to be approximately given by

$$\tau \approx \frac{2\sqrt{2k_2}k_3 h^{\frac{1}{4}}}{u}, \tag{3}$$

in which $k_2$ is a constant dependent on the ratio of specific heats within the atmosphere $\gamma$ and the Mach number $M$:

$$k_2 = \frac{(\gamma+1)M^4}{\sqrt{2}(M^2-1)^{\frac{3}{4}}}, \tag{4}$$

and $k_3$ is a constant related to the capsule's geometry,

$$k_3 = \delta l^{\frac{3}{4}}, \tag{5}$$

in which $\delta$ is the ratio of maximum effective capsule radius to capsule length $l$.

For the ORX capsule with radius 0.4 m and length 0.5 m, $k_3 = 0.48$ (noting that in practice, the effective radius of the capsule may be larger due to shockwave stand-off).

TABLE 1
**Meteorological Data Recorded by the Nevada Department of Transport Weather Station at U.S. 50 Bean Flats Rest Area at 14:46:00 UTC**

| Variable | Value |
|---|---|
| Air temperature | +4.5°C |
| Surface temperature | +8.2°C |
| Dewpoint | −3.3°C |
| Relative humidity | 56% |
| Wind direction | 302° |
| Wind speed | 0.0 m/s |
| Gust direction | 291° |
| Gust speed | 0.22 m/s |
| Precipitation | None |

Data are shared as provided; surface temperature has been averaged over two sensors.

Given the nominal prelanding predictions of $h$ = 62,000 m and $u$ = 10,800 m/s, and assuming a canonical $\gamma = 1.4$ (as per Kanamori *et al.*, 1992, though it is likely lower at $M$ = 30), we derive $k_2 \approx 8370$. Using the "effective" (slant) height makes little difference to this calculation given that the capsule is almost directly overhead.

These results yield an estimate of $\tau = 0.18$ s. This is in remarkably close agreement with our measured value of 0.15 s given the significant simplifications made in the calculation of the constants above and the unknown capsule height and atmospheric conditions at the time of overflight. Calculation of a more accurate ratio of specific heats or applying a correction for atmospheric structure and wind structure may enable an even more accurate match.

Kanamori *et al.* (1992) also gives an approximate relation for theoretical overpressure as a function of aspect ratio and altitude:

$$\frac{\Delta P}{P} \approx k_1 k_3 h^{-\frac{3}{4}}, \tag{6}$$

in which $k_1$ is another constant given by

$$k_1 = \frac{2^{\frac{1}{4}}\gamma}{(\gamma+1)^{\frac{1}{2}}}(M^2-1)^{\frac{1}{8}}. \tag{7}$$

We compute $k_1 = 2.5$ and hence $\frac{\Delta P}{P} = 0.00030$. Based on a receiver altitude of 1920 m and an ambient air temperature of +4.5°C, $P$ = 79,600 Pa and hence $\Delta P \approx 24$ Pa. We are not able to directly compare this to the actual overpressure as the ground compliance at the array site was not measured.

However, we note that the theoretical overpressure is still significantly larger than that recorded by Fernando *et al.* (2024) of 0.7 Pa at the Fish Creek site ∼50 km away. Computing the expected overpressure at Fish Creek while accounting for the longer slant height at this laterally offset station yields a predicted overpressure of 21 Pa, still around 30 times too large.

Therefore, we conclude that this formula for $\Delta P$ is not valid in this regime. This may due to the capsule's hypersonic speed producing a substantially modified bow shock, or its extreme altitude producing different interactions with the surrounding airflow, as compared to tests conducted at lower altitudes and lower Mach numbers.

## Ancillary data

We will briefly discuss ancillary data which was collected as part of this deployment by part of a team of volunteers, working remotely with data provided online by the Nevada Department of Transport (NVDOT). All these data, and similar readings from nearby potentially of interest to other portions of the ORX EDL instrumentation campaign, are available in our online repository (see Data and Resources for link).

**Weather data.** The proximity of the array to U.S. Highway 50 ("The Loneliest Road in America") had the advantage that meteorological data could be sourced from a nearby NVDOT weather station. This station ("US50 Bean Flats Rest Area") was only 275 m from the array centerpoint. The closest reading to the capsule's overflight and the arrival of the sonic boom was made at 14:44:00 UTC, with measurements shown in Table 1.

While the lack of wind during this period represents only a single measurement at the surface, it may be indicative of a quiescent planetary boundary layer at the time in question. This may have led to less turbulent dissipation of the wavefront (one of the sources of rounding in the $N$ wave).

## Traffic data

We also made use of the traffic camera installed at the Bean Flats Rest area to record traffic movements, with the aim of being able to identify contamination in the ORX signal if needed.

Data for around five minutes before and after the overflight are given in Table 2. Because the traffic camera feeds are not archived, multiple volunteers were asked to record vehicles passing the array in real time, thereby eliminating some of random the error associated with streaming lag (we find a systematic error of around 40 s delay in video data as compared to when a vehicle becomes apparent in the seismic data). The data provided is a synthesis of that from all volunteers, with the lower, mean, and upper bounds on vehicle passage times given. The streaming lag has not been corrected for in Table 2.

In two cases, the vehicle may have been towing a trailer, but this could not be determined due to poor video resolution. To corroborate readings between different volunteers who recorded slightly different vehicle arrival times due to

TABLE 2
**Traffic Data Recorded by the Cameras at the U.S. 50 Bean Flat Rest Area**

| UTC Time–Lower Bound (hh:mm:ss) | UTC Time–Mean (hh:mm:ss) | UTC Time–Upper Bound (hh:mm:ss) | Direction | Speed | Type |
|---|---|---|---|---|---|
| 14:39:26 | 14:39:47 | 14:40:03 | Away | Medium/fast | Car |
| 14:41:23 | 14:41:35 | 14:41:53 | Toward | Medium | Car (with trailer?) |
| 14:41:38 | 14:41:39 | 14:41:39 | Toward | Medium | Car (with trailer?) |
| 14:47:49 | 14:47:57 | 14:48:00 | Away | Slow/stationary | Lorry/truck |
| 14:51:47 | 14:51:52 | 14:52:00 | Towards | Medium/slow | Car with trailer |

Note that "Away" and "Toward" refer to whether the vehicle was moving away from (westbound) or toward (eastbound) relative to the westward-facing traffic camera. Speeds were judged by each relative to the average in the 30 min or so preceding the interval of interest.

streaming lag, car color was also recorded; but this is not noted in Table 2 as it is not relevant to seismic observations.

As per Table 2, no moving vehicles were noted at 14:46 UTC, when the ORX signal was detected. A truck which passed the camera at 14:47 UTC was identified in the seismic dataset as being a source of noise beginning at 14:45:50 UTC, and extending out to 14:49 UTC. Given this long duration, and its slow speed observed in the video data, we suspect it was idling in the layby prior to driving away.

## Summary

Seismic signatures associated with the EDL of the OSIRIS-REx spacecraft were recorded by an 11-instrument seismic array located almost immediately under the point of peak heating over northern Nevada.

A classic rounded *N* wave, characteristic of a decayed sonic boom, is observed propagating across the array. The entire *N* wave (compression and rarefaction) lasts ~0.15 s, with the compressional wave extending to higher frequencies (up to at least ~450 Hz at some stations) than the rarefaction (~40 Hz). The measured duration of the *N* wave is in very good agreement with theoretical predictions.

The wavefront's moveout across the array is predominantly in the downrange direction (at an azimuth of 253°, close to the prelanding prediction of 249°. The wave is also propagating almost vertically downward (around 4° from the vertical). Following the *N* wave, a set of seismic postcursors are recorded, likely some combination of air-coupled seismic waves, additional (slower) airwaves, and long-period ground deformation induced by the initial wavefront.

Data from this array are able to exclude the spacecraft being well south of its nominal trajectory. Analysis of the apparent slowness of the *N* wave across the array also indicates an equivalent point-source origin which is almost exactly overhead in both the uprange–downrange and crossrange planes.

Further work would likely enable a more thorough inversion of the capsule's trajectory, accounting for the extended nature of the source and the effects of refraction arising from atmospheric stratification. This would enable this dataset to be used as a more reliable test case for trajectory determinations of natural meteoroids using their seismic signatures.

## Data and Resources

Deployment locations and ancillary data (weather and traffic data) are available via this Zenodo repository: doi: 10.5281/zenodo.12210877. Seismic data are available from the FDSN under network code 2X (Fernando *et al.*, 2023) at doi: 10.7914/8ZEK-PE59.

## Declaration of Competing Interests

The authors acknowledge that there are no conflicts of interest recorded.

## Acknowledgments

The authors are most grateful to the National Aeronautics and Space Administration's (NASA) Scientifically Calibrated In-Flight Imagery (SCIFLI) team for facilitating the fieldwork component of this expedition and to the townspeople of Eureka, Nevada, for their hospitality. They are also grateful to the Nevada Department of Transport (NVDOT) for the free access to traffic and meteorological data. B. F. is funded by the Blaustein Fellowship in Earth and Planetary Sciences at Johns Hopkins University. J. W. was funded by the Miller Institute for Basic Research in Science at UC Berkeley. C. C. is funded by the United Kingdom Space Agency Fellowship in Mars Exploration Science under ST/Y005600/1. T. C. thanks the Royal Society for funding under URF\R\231019.

## References

Ajluni, T., D. Everett, T. Linn, R. Mink, W. Willcockson, and J. Wood (2015). OSIRIS-REx, returning the asteroid sample, *2015 IEEE Aerospace Conference*, IEEE, Big Sky, Montana, 7–14 March 2015.

Allander, K. K., and D. L. Berger (2009). Seismic velocities and thicknesses of alluvial deposits along Baker Creek in the Great Basin National Park, east-central Nevada, *U.S. Geol. Surv. Open-File Rept. 2009-1174*.

Ben-Menahem, A., and S. J. Singh (1981). *Seismic Waves and Sources*, Springer Science & Business Media, New York.

Carlson, H. W., and D. J. Maglieri (1972). Review of sonic-boom generation theory and prediction methods, *J. Acoust. Soc. Am.* **51,** no. 2C, 675–685.

Cates, J. E., and B. Sturtevant (2002). Seismic detection of sonic booms, *J. Acoust. Soc. Am.* **111,** no. 1, 614–628.

Cook, J. C., and T. T. Goforth (1970). Ground motion from sonic booms, *J. Aircr.* **7,** no. 2, 126–129.

Edwards, W. N., D. W. Eaton, and P. G. Brown (2008). Seismic observations of meteors: Coupling theory and observations, *Rev. Geophys.* **46,** no. 4, doi: 10.1029/2007RG000253.

Fernando, B., C. Charalambous, C. Saliby, E. Sansom, C. Larmat, D. Buttsworth, D. Hicks, R. Johnson, K. Lewis, M. McCleary, *et al.* (2024). Seismoacoustic measurements of the OSIRIS-REx re-entry with an off-grid Raspberry PiShake, *Seismica* **3,** no. 1, doi: 10.26443/seismica.v3i1.1154.

Fernando, B., C. Charalambous, and N. Schmerr (2023). Array-based seismic measurements of OSIRIS-REx's re-entry, doi: 10.31223/X51D7H.

Fernando, B., N. Wójcicka, M. Froment, R. Maguire, S. C. Stähler, L. Rolland, G. S. Collins, O. Karatekin, C. Larmat, E. K. Sansom, *et al.* (2021). Listening for the landing: Seismic detections of Perseverance's arrival at Mars with InSight, *Earth Space Sci.* **8,** no. 4, e2020EA001585, doi: 10.1029/2020EA001585.

Fernando, B., N. Wójcicka, Z. Han, A. Stott, S. Ceylan, C. Charalambous, G. S. Collins, D. Estévez, M. Froment, M. Golombek, *et al.* (2021). Questions to heaven, *Astron. Geophys.* **62,** no. 6, 6–22.

Fernando, B., N. Wójcicka, R. Maguire, S. C. Stähler, A. E. Stott, S. Ceylan, C. Charalambous, J. Clinton, G. S. Collins, N. Dahmen, *et al.* (2022). Seismic constraints from a Mars impact experiment using InSight and perseverance, *Nat. Astron.* **6,** no. 1, 59–64.

Kanamori, H., J. Mori, B. Sturtevant, D. Anderson, and T. Heaton (1992). Seismic excitation by space shuttles, *Shock Waves* **2,** 89–96.

Karakostas, F., V. Rakoto, P. Lognonne, C. Larmat, I. Daubar, and K. Miljković (2018). Inversion of meteor rayleigh waves on earth and modeling of air coupled rayleigh waves on Mars, *Space Sci. Rev.* **214,** 1–33.

Kenda, B., M. Drilleau, R. F. Garcia, T. Kawamura, N. Murdoch, N. Compaire, P. Lognonné, A. Spiga, R. Widmer-Schnidrig, P. Delage, *et al.* (2020). Subsurface structure at the insight landing site from compliance measurements by seismic and meteorological experiments, *J. Geophys. Res.* **125,** no. 6, doi: 10.1029/2020JE006387.

McDonald, J. A., and T. T. Goforth (1969). Seismic effects of sonic booms: Empirical results, *J. Geophys. Res.* **74,** no. 10, 2637–2647.

Pierce, A. D., and D. J. Maglieri (1972). Effects of atmospheric irregularities on sonic-boom propagation, *J. Acoust. Soc. Am.* **51,** no. 2C, 702–721.

Plotkin, K. J. (2002). State of the art of sonic boom modeling, *J. Acoust. Soc. Am.* **111,** no. 1, 530–536.

ReVelle, D., and W. Edwards (2007). Stardust—An artificial, low-velocity "meteor" fall and recovery: 15 January 2006, *Meteorit. Planet. Sci.* **42,** no. 2, 271–299.

ReVelle, D., W. Edwards, and T. Sandoval (2005). Genesis—An artificial, low velocity "meteor" fall and recovery: September 8, 2004, *Meteorit. Planet. Sci.* **40,** no. 6, 895–916.

Rost, S., and C. Thomas (2002). Array seismology: Methods and applications, *Rev. Geophys.* **40,** no. 3, 2-1–2-27.

Sansom, E. K., H. A. Devillepoix, M.-Y. Yamamoto, S. Abe, S. Nozawa, M. C. Towner, M. Cupák, Y. Hiramatsu, T. Kawamura, K. Fujita, *et al.* (2022). The scientific observation campaign of the Hayabusa-2 capsule re-entry, *Publ. Astron. Soc. Jpn.* **74,** no. 1, 50–63.

Silber, E. A., D. C. Bowman, and S. Albert (2023). A review of infrasound and seismic observations of sample return capsules since the end of the Apollo era in anticipation of the OSIRIS-REx arrival, *Atmosphere* **14,** no. 10, 1473, doi: 10.3390/atmos14101473.

Silber, E. A., D. C. Bowman, C. G. Carr, D. P. Eisenberg, B. R. Elbing, B. Fernando, M. A. Garcés, R. Haaser, S. Krishnamoorthy, C. A. Langston, *et al.* (2024). Geophysical observations of the 24 September 2023 OSIRIS-REx sample return capsule re-entry, doi: 10.48550/arXiv.2407.02420.

Sorrells, G. G. (1971). A preliminary investigation into the relationship between long-period seismic noise and local fluctuations in the atmospheric pressure field, *Geophys. J. R. Astron. Soc.* **26,** nos. 1/4, 71–82.

Whitham, G. B. (1974). *Linear and Nonlinear Waves*, John Wiley & Sons, New York.

Yamamoto, M.-Y., Y. Ishihara, Y. Hiramatsu, K. Kitamura, M. Ueda, Y. Shiba, M. Furumoto, and K. Fujita (2011). Detection of acoustic/infrasonic/seismic waves generated by hypersonic re-entry of the HAYABUSA capsule and fragmented parts of the spacecraft, *Publ. Astron. Soc. Jpn.* **63,** no. 5, 971–978.

## Authors and Affiliations

**Benjamin A. Fernando:** Department of Earth and Planetary Sciences, Johns Hopkins University, Baltimore, Maryland, U.S.A., https://orcid.org/0000-0002-7321-8401; **Constantinos Charalambous:** Department of Electrical and Electronic Engineering, Imperial College London, London, United Kingdom, https://orcid.org/0000-0002-9139-3895; **Nick Schmerr:** Department of Geology, University of Maryland, Maryland, U.S.A., https://orcid.org/0000-0002-3256-1262; **Timothy J. Craig:** Institute of Geophysics and Tectonics, School of Earth and Environment, University of Leeds, Leeds, United Kingdom; **Jonathan Wolf:** Department of Earth and Planetary Sciences, University of California, Berkeley, California, U.S.A. Miller Institute for Basic Research in Science, Berkeley, California, U.S.A.; **Kevin Lewis:** Department of Earth and Planetary Sciences, Johns Hopkins University, Baltimore, Maryland, U.S.A., https://orcid.org/0000-0003-3412-803X; **Eleanor K. Sansom:** International Centre for Radio Astronomy Research, Space Science and Technology Centre, Curtin University, Perth, Western Australia, Australia Space Science and Technology Centre, School of Earth and Planetary Science, Curtin University, Perth, Australia, https://orcid.org/0000-0003-2702-673X; **Christelle Saliby:** Observatoire de la Côte d'Azur, Université Côte d'Azur, CNRS, IRD, Géoazur, Valbonne, France, https://orcid.org/0000-0002-0101-723X; **Meaghan McCleary:** Analytical Mechanics Associates, Inc./NASA Langley Research Center, Hampton, Virginia, U.S.A., https://orcid.org/0009-0008-5233-2820; **Jennifer Inman:** NASA Langley Research Center, Hampton, Virginia, U.S.A., https://orcid.org/0000-0001-6213-3181; **Justin LaPierre:** Sandia National Laboratories, Albuquerque, New Mexico, U.S.A.; **Miro Ronac Giannone:** Department of Earth Sciences, Southern Methodist University, Dallas, Texas, U.S.A., https://orcid.org/0000-0001-8752-2263; **Karen Pearson:** Independent Researcher, Bowie,

Maryland, U.S.A.; **Michael Fleigle:** Sandia National Laboratories, Albuquerque, New Mexico, U.S.A.; **Carene Larmat:** Los Alamos National Laboratory, Los Alamos, New Mexico, U.S.A.; **Ozgur Karatekin:** Royal Observatory of Belgium, Uccle, Belgium, https://orcid.org/0000-0003-0153-7291; **Lavender Elle Hanson:** Department of Earth and Planetary Sciences, Johns Hopkins University, Baltimore, Maryland, U.S.A., https://orcid.org/0000-0003-2298-8382; **Shivani Baliyan:** Independent Researcher, Boulder, Colorado, U.S.A.; **David Buttsworth:** Institute for Advanced Engineering and Space Sciences, University of Southern Queensland, Queensland, Australia; **Hiu Ching Jupiter Cheng:** Department of Geological Sciences, University of Alabama, Tuscaloosa, Alabama, U.S.A.; **Neeraja S. Chinchalkar:** University of Western Ontario, London, Ontario, Canada, https://orcid.org/0000-0002-3541-3791; **Luke Daly:** School of Geographical and Earth Sciences, University of Glasgow, Glasgow, United Kingdom, https://orcid.org/0000-0002-7150-4092; **Hadrien A. R. Devillepoix:** Institute of Geophysics and Tectonics, School of Earth and Environment, University of Leeds, Leeds, United Kingdom, https://orcid.org/0000-0001-9226-1870; **Aly Muhammad Gajani:** Institute of Space Science and Technology, University of Karachi, Karachi, Pakistan, https://orcid.org/0009-0001-5249-9873; **Carina T. Gerritzen:** Archaeology, Environmental Changes & Geo-Chemistry, Vrije Universiteit Brussel, Brussels, Belgium, https://orcid.org/0000-0002-1494-2643; **Harish :** Laboratory for Atmospheric and Space Physics, University of Colorado, Boulder, Colorado, U.S.A., https://orcid.org/0000-0002-4152-4295; **Daniel C. Hicks:** U.S. Department of Defense (KBR Consultant), Las Cruces, New Mexico, U.S.A.; **Roy Johnson:** NASA Ames Research Center, Moffett Field, California, U.S.A.; **Sabrina Y. Khan:** Department of Earth and Planetary Sciences, Johns Hopkins University, Baltimore, Maryland, U.S.A.; **Sarah N. Lamm:** Earth, Energy, and Environment Centre, University of Kansas, Lawrence, Kansas, U.S.A., https://orcid.org/0000-0003-3810-1213; **Cara Pesciotta:** Department of Earth and Planetary Sciences, Johns Hopkins University, Baltimore, Maryland, U.S.A., https://orcid.org/0009-0007-6910-6347; **Tom Rivlin:** Atominstitut, Technische Universität Wien, Vienna, Austria, https://orcid.org/0000-0002-9275-2917; **Lucie Rolland:** Laboratoire Géoazur, Université de Nice Côte d'Azur, Nice, France, https://orcid.org/0000-0002-5197-963X; **Maxwell Marzban Thiemens:** Department of Geosciences, University of Edinburgh, Edinburgh, Scotland, https://orcid.org/0000-0002-7835-4402; **Alice R. Turner:** Institute for Geophysics, University of Texas, Austin, Texas, U.S.A., https://orcid.org/0000-0002-3743-6428; and **Fabian Zander:** Institute for Advanced Engineering and Space Sciences, University of Southern Queensland, Queensland, Australia

**Manuscript received 24 August 2024**
**Published online 12 February 2025**